Generation of negative acoustic radiation forces

Mohamed A. Ghanem[1]

[1]Center for Industrial and Medical Ultrasound, Applied Physics Laboratory, University of Washington, Seattle, WA 98105 USA

Acoustic beam

A focused 256-element array operating at 1.5 MHz is used to create the acoustic beams used for generating negative radiation forces. The phase and amplitude of each element are independently controlled. The array elements are arranged along 16 spirals distributed on a spherical surface with a radius of curvature of 12 cm. Spherical basis used to describe the radiation forces on a sphere centered at the focus of spherical coordinates is shown in Figure S1. The velocity potential can be expanded using a spherical basis given by [1]:

$$\psi(r,\theta,\phi) = \psi_0 A_n^m j_n(kr)\, e^{im\phi} P_n^m(\cos\theta). \qquad \text{(S1)}$$

r, θ, and ϕ are the spherical basis, ψ_0 is real amplitude constant, A_n^m are beam coefficients, j_n is spherical Bessel function of degree n, and P_n^m is associate Legendre polynomial of degree *n* and order *m*.

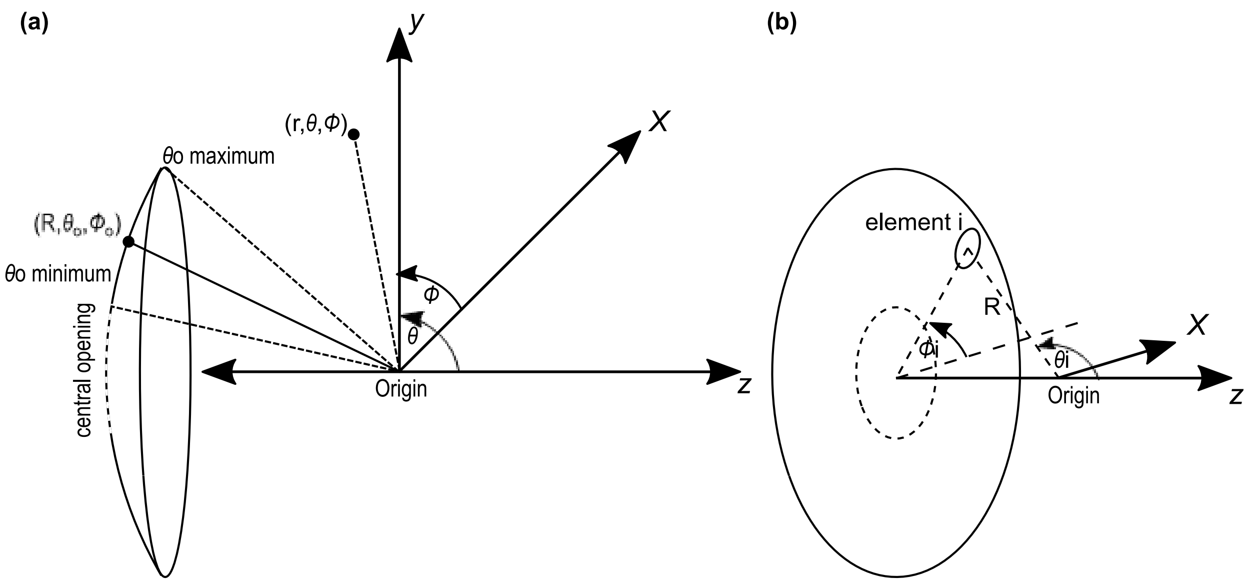

Figure S1: Spherical coordinates used to define the spherical basis. The coordinates of a point on the transducer's spherical surface are defined in (a) with a focusing angle of θ_0-maximum. The θ range used to define the associate Legendre polynomial over the transducer aperture is between θ_0-minimum to θ_0-maximum. The coordinates of each element of the transducer array are defined in (b) with coordinates (R,θ_i,ϕ_i).

An observation point in the basis is defined by coordinates (r,θ,ϕ) and a point on the transducer is defined by (R,θ_o,ϕ_o), where R is the radius of curvature. The center of element *i* is located at (R,θ_i,ϕ_i). Vortex beams are generated by imposing an azimuthal phase variation corresponding to integer multiples of the azimuthal angle from 0 to 2π through the term $e^{im\phi}$, where m is the topological charge. The phase assigned to element i is $\phi_\mathrm{i} = m \times \mathrm{atan}(y_i/x_i)$ where $(x, y, z)_\mathrm{i}$ are its cartesian coordinates.

While vortex beams are associated with azimuthal coordinate (ϕ), the interference patterns to generate pulling radiation forces are produced by additionally modulating the incident beam in the elevation coordinate (θ) using the $P_n^m(\cos\theta)$ term. The elevation angle of array element i is defined as $\theta_i = \mathrm{asin}(\sqrt{x_i^2 + y_i^2}/R)$. Since the array consists of 16 identical spirals with the same angular distribution, the associated Legendre polynomial is calculated for a single spiral and replicated across the remaining spirals.

The associated Legendre polynomial term determines relative amplitude of each array elements. The polynomial output is normalized by its maximum value. Rather than applying the continuous normalized amplitudes, each element's amplitude is discretized to either 1 or -1 relative to its full output. Elements with positive amplitudes are assigned to a complex factor $e^{(im\phi + 0)}$, while those with negative amplitudes are assigned $e^{i(m\phi + \pi)}$, indicating a phase difference of π between both groups (Figure S2).

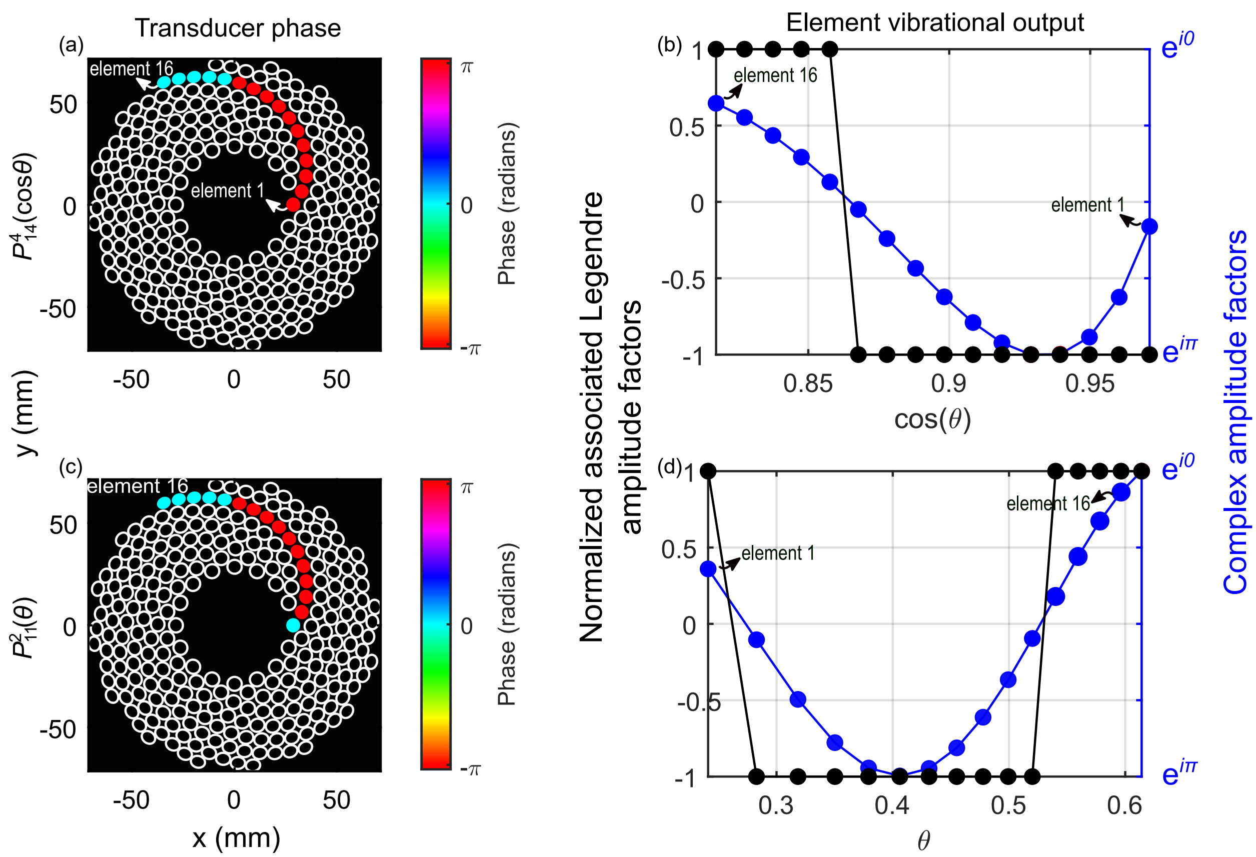

Figure S2: The transducer phase for each 16-element spiral for the associated Legendre polynomials (a and c). The associated Legendre polynomials output is normalized by the absolute maximum value (b and d), then the complex amplitude is defined as e^{i0} and $e^{i\pi}$ which is a π-phase difference to control the sign. Associated Legendre $P_{14}^4(\cos\theta)$ is shown in (b) and the artificially modified argument from $\cos\theta$ to θ in $P_{11}^2(\theta)$ is shown in (d). The goal was to change the phase of the inner elements to 0 to impose a smooth transition and optimize the beam interference pattern. Elements on the inner ring are the innermost elements, and elements on the outer ring are the outermost elements.

The spherical basis of equation (S1) is formally defined over the full polar range for $\theta \in [0, \pi]$ (0°–180°). When equation (S1) is used to define the boundary condition on the transducer surface, the active aperture occupies only a limited elevation span, $\theta \in [14°, 35°]$, with the pressure constrained to be zero elsewhere. No single associated Legendre polynomial satisfies this truncated boundary condition. Therefore, only sections of the polynomials that fall within the transducer active aperture are considered, regardless of their behavior outside the active aperture. Over this reduced range, several associated Legendre polynomials satisfy the elevation dependence, as illustrated in Figure S3 for various combinations of *n* and *m* for $P_n^m(\cos\theta)$ that produce nearly identical profiles within the transducer aperture. This non-uniqueness relaxes the constraint $m \leq |n|$ otherwise required for the spherical harmonic expansion in equation (S1) [2]. As a result, the topological charge *m* in the azimuthal term $e^{im\phi}$ is replaced by an independent topological charge *M* yielding the term $e^{iM\phi}$, which is distinct from the order *m* of $P_n^m(\cos\theta)$. Furthermore, since the amplitude values are mapped to relative phase delays between the elements, the set of equivalent associated Legendre polynomials over the transducer aperture is further expanded because polynomials mirrored about the *y*-axis produce identical relative phase assignments between elements and are therefore interchangeable for beam synthesis purposes (Figure S3).

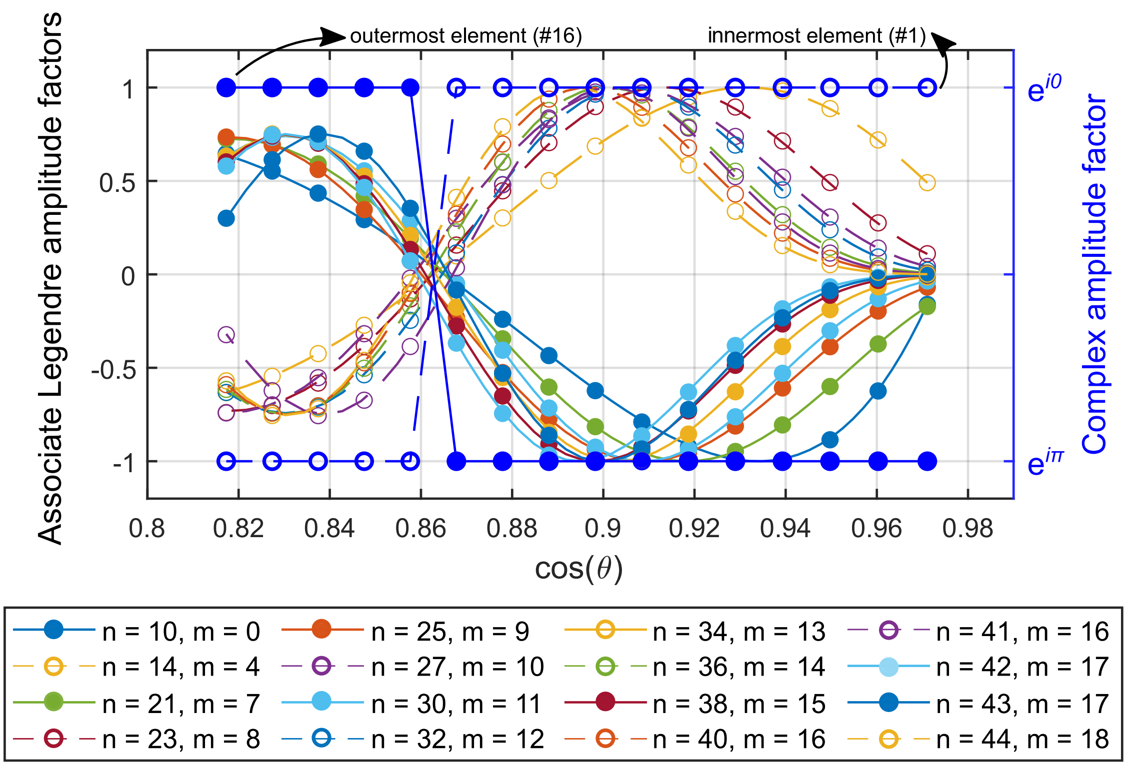

Figure S3: Combinations of several $P_n^m(\cos\theta)$ that match the distribution of $P_{14}^4(\cos\theta)$ over the physical transducer aperture. The polynomials are amplitude factors that are normalized, then converted to amplitudes of 1 or -1, which are mapped to a complex amplitude of e^{i0} or $e^{i\pi}$, which is a π phase difference between the elements on each spiral.

To optimize the beam interference pattern and suppress strong secondary lobes, we searched for a $P_n^m(\cos\theta)$ whose phase increases smoothly from zero at the innermost element, reaches π at the central elements in the central area, and returns to zero at the outermost boundary. No polynomial satisfying this condition was found over the transducer aperture. Therefore, we artificially modified the polynomial argument from cos θ to θ, granted that all element elevation coordinates θ_i satisfy $|\theta_i| \leq 1$. This substitution serves as an initial point to guide the beam search more efficiently. It is worth noting that while the smooth amplitude variation of the associated Legendre polynomials (Figure S2 b and d) reduces secondary lobes, it also diminishes the acoustic power output and consequently the radiation forces. Therefore, we utilized the full output of the elements to maximize the radiation forces.

The interference pattern produced by the Legendre elevation term creates a destructive interference region that splits the axial pressure, analogous to the acoustic field produced by two or more concentric focused transducers that are driven π out of phase [3] (Figure S4). The beam pattern can be understood as arising from interference between several vortices created by different radial sections of the array with each section having a unique focusing angle. The innermost ring of elements produces a vortex beyond the geometric focus, while the outermost ring of elements produces a vortex proximal to the geometric focus. The interference between these pre-focal and post-focal vortices produces a wider diameter near the acoustic focus, resulting in a larger trap waist. This fusiform-shaped beam bends around targets, leading to minimal backscattering and increased forward scattering as the target nears the narrow beam end farther from the source.

The topological charge *M* controls the diameter of the vortex beam linearly [4] and simulations confirm that *M* also governs the waist size of the presented pulling beams (Figure S5), as descried by the mechanism mentioned above. A larger *M* can impart pulling forces on larger targets, but the vortices diffract over a larger section, reducing the intensity and weakening the interference pattern. Simulations show that radiation forces become insufficient to produce meaningful pulling beyond $M \geq 6$.

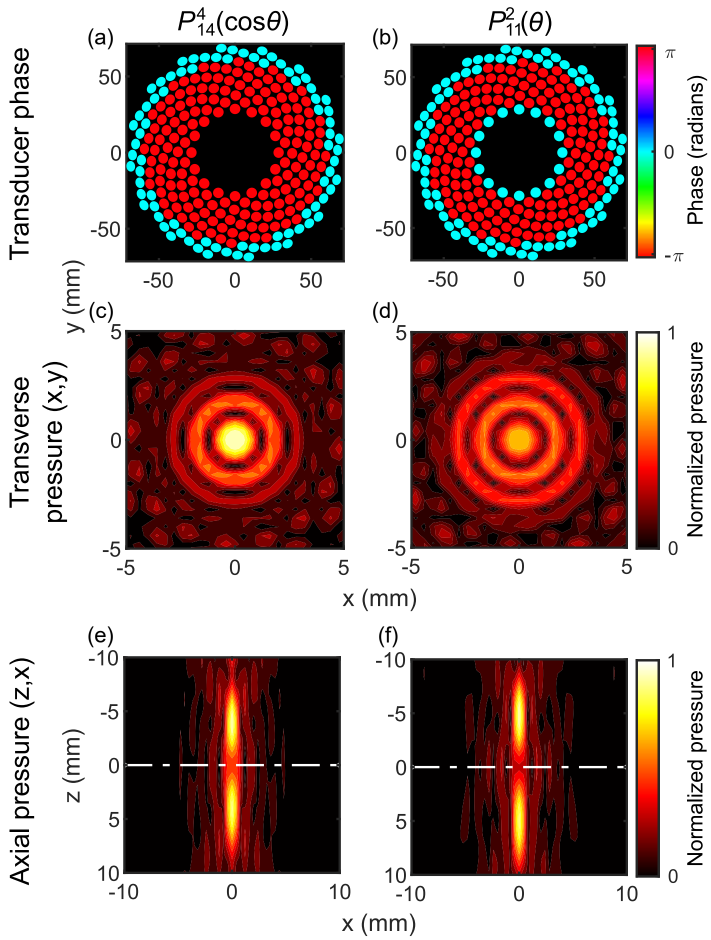

Figure S4: Simulations of pressure distribution from the associated Legendre $P_{14}^4(\cos\theta)$ (a, c, and e) and modified associated Legendre term $P_{11}^2(\theta)$ (b, d, and f). The transducer phase (a and b) produces a pressure interference (c – f), analogous to concentric focused transducers that are π out-of-phase.

The phase from vortex beam produces a helical wavefront (Figure S5 a-c) that can transfer angular momentum and spin objects[5]. Since radiation torque, like radiation force, is an average quantity, it can be eliminated by transmitting two consecutive pulses with opposite topological charges[6–8]. The phase assigned to each element *i* for beam synthesis is:

$\psi_i^1 = M \times \mathrm{atan}(y_i/x_i) + P_n^m(f(\theta_i))$, and $\psi_i^2 = -M \times \mathrm{atan}(y_i/x_i) + P_n^m(f(\theta_i))$,

for the 1st and 2nd pulses, respectively. The first term in the azimuthal phase for the vortex, and the second term is phase derived from the associated Legendre polynomial, where $f(\theta)$ is equal to either $\cos(\theta)$ or θ as in Figure S2. This pulsing scheme is used throughout the manuscript for all beams with topological charge M.

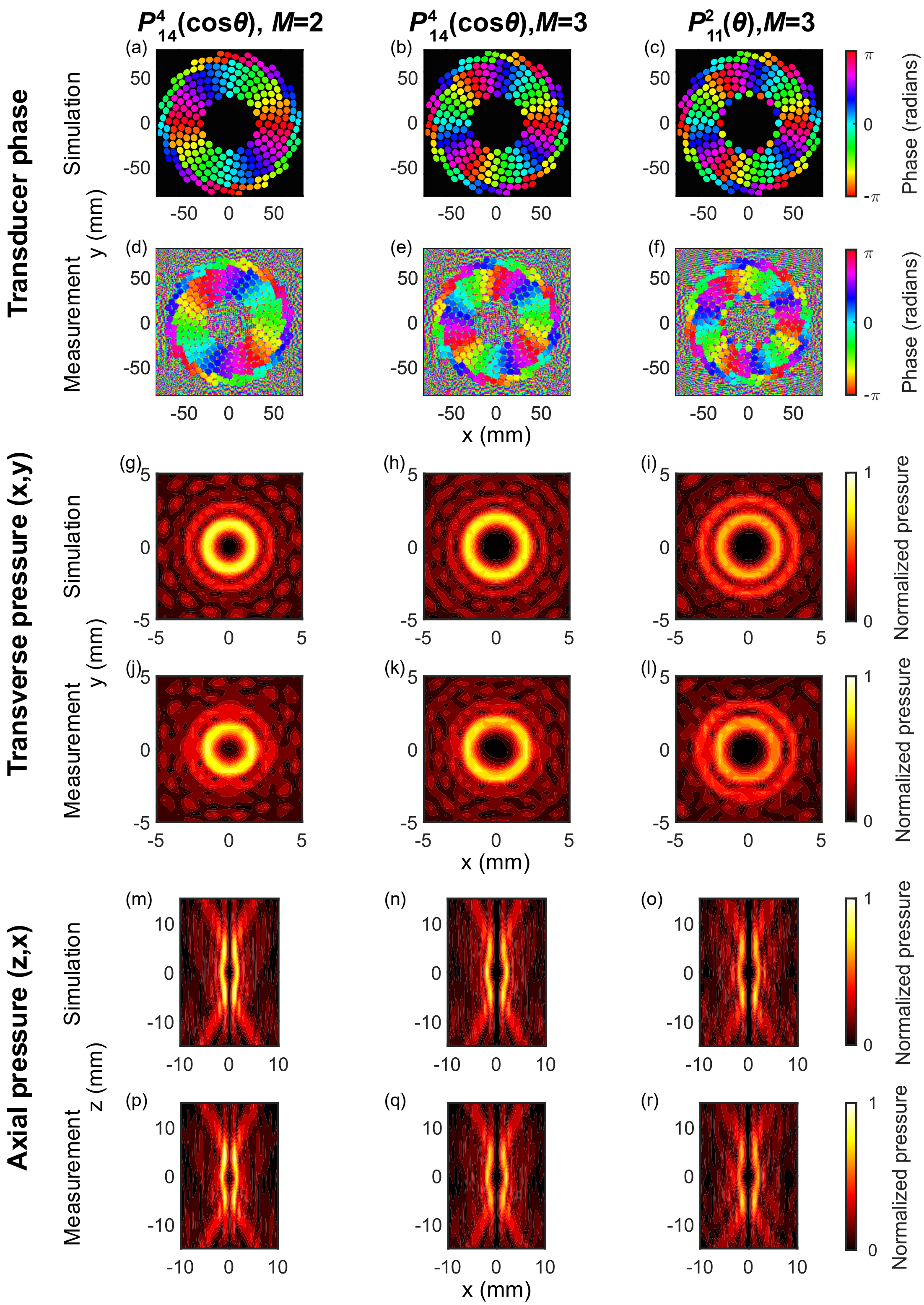

Figure S5: Generation of the acoustic trap for the $P_{14}^{4}(\cos\theta)$ with M = 2 (left column), $P_{14}^{4}(\cos\theta)$ with M = 3 (middle column), and $P_{11}^{2}(\theta)$ with M = 3. Transducer phase (a-c) is compared to experimental phase (d-f) from holography scan. The normalized pressure amplitude for all three beams in the *xy*-transverse plane (g-i) shows that larger M produces larger beam diameter, while the *zx*-axial plane (m-r) shows the fusiform-shaped beams as the beams are narrow at the ends with a wider waist in the center. The experimental values are from the propagation of the holography scan to different z locations.

Field measurements

The pressure field was scanned with a 200-μm diameter capsule hydrophone (HGL-0200, Onda Corp., CA, USA) in a square grid with a spacing of 0.5mm ($\lambda/2$). The scan plane size was 88×88 mm and positioned 40 mm proximal to the focus. A continuous wave (CW) analysis was used to record the acoustic hologram and reconstruct the complex pressure in three-dimensional space. The angular spectrum at the scan plane z_s was defined as:

Error! Hyperlink reference not valid. $S(k_x, k_y) = \int_{-\infty}^{\infty}\int_{-\infty}^{\infty} p(x,y)\, e^{-ik_x x - ik_y y} dx\, dy,$

then the hydrophone directivity correction $D\left(k_x, k_y\right)|_{f=1.5\ MHz}$ from [9], was applied to obtain:

Error! Hyperlink reference not valid. $S_{corr}(k_x, k_y) = \frac{S(k_x,k_y)}{D(k_x,k_y)|_{f=1.5\ MHz}},$

which was used to construct the complex pressure at a plane normal to the acoustic axis located at z_i:

$$p(x, y, z_i) = \frac{1}{4\pi^2} \iint_{k_x^2+k_y^2 \le k^2} S_{corr}(k_x, k_y)\, e^{ik_x x + ik_y y + i\sqrt{k^2-k_x^2-k_y^2}\,(z_i - z_s)}\, dk_x dk_y \tag{S2}$$

where k is the wavenumber. For a harmonic wave, the particle velocity is defined as:

$$\mathbf{v} = \frac{\nabla p}{i\omega\rho}$$

Accordingly, the j^{th} component of the velocity vector from equation (S2) is:

$$\mathrm{v}_j(x, y, z_i) = \frac{1}{4\pi^2 c\rho} \iint_{k_x^2+k_y^2 \le k^2} \frac{k_j}{k} S_{corr}(k_x, k_y)\, e^{ik_x x + ik_y y + ik_z(z_i - z_s)}\, dk_x dk_y. \tag{S3}$$

Acoustic radiation forces ARF

The ARFs on a given scatterer are calculated by integrating the change in wave momentum flux over a closed surface S enclosing the scatterer. This integral is defined as

$\mathbf{F} = \oiint_{S} \frac{d\mathbf{F}}{dS} dS$

where the force per unit area, $\frac{d\mathbf{F}}{dS}$, is expressed as:

$$\frac{d\mathbf{F}}{dS} = \left(\frac{\rho|\mathbf{v}|^2}{4} - \frac{|p|^2}{4\rho c^2}\right)\mathbf{n} - \frac{\rho}{2}\mathrm{Re}[\mathbf{v}^*(\mathbf{v}\cdot\mathbf{n})].$$

Here, **n** is the unit normal to the surface element dS, ρ and c are the medium density and speed of sound, and asterisks denote complex conjugates. The total pressure p and total velocity $\boldsymbol{v}$ each consist of the incident field, determined from holography measurements via equations (S2) and (S3), and the scattered field, obtained by multiplying the incident values by the appropriate spherical scattering coefficients. The ARFs are calculated using an angular spectrum decomposition approach presented in reference [10] and the full ARF definitions are detailed in Appendix A.

1. Two negative ARF regimes: small (ka<1) vs large (ka≥1) objects

Using the pressure and particle velocity based on our holography scan from equations (S2) and (S3), the radiation forces are calculated along the acoustic axis z for glass spheres of varying diameters. For each sphere diameter, the forces are normalized so that the largest negative force at a given axial location equals the weight of the sphere.

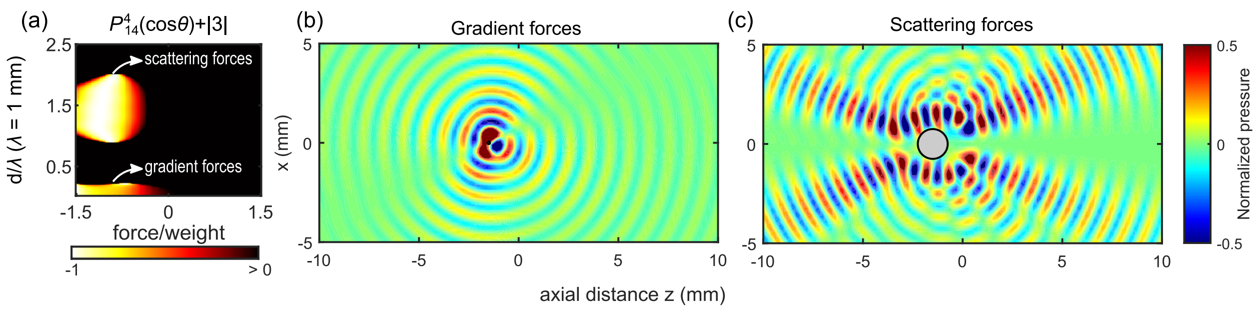

Figure S6: Negative radiation force that pull targets with two different mechanisms: (a) gradient (b) and non-conservative (c) forces. For the subwavelength particles, gradient forces (b) on a 0.125 mm glass sphere impart pulling as result of the convergent wavefronts onto the particle. For larger objects, non-conservative forces (c) are the dominant mechanism on 1.5 mm glass sphere. For target is located at z = -1.5 mm for both cases (b) and (c).

Two distinct regions govern the mechanisms of generated negative radiation forces depending on the target size (Figure S6). For particles much smaller than the acoustic wavelength λ, the dominant mechanism is the gradient forces arising from the wavefronts converging onto the particle. For targets comparable to or larger than λ, the dominant mechanism is scattering or absorption of the wave by the target. The total pressure field – incident and scattered – in each region is shown in Figure S6b and c for a 0.125 mm and a 1.5 mm glass spheres, respectively, both located near the acoustic focus at z = -1.5 mm. To investigate this separation of mechanisms, the cumulative sum of the acoustic radiation force along the acoustic axis is plotted against the series sum of the ARF multipole expansion over index n (Figure S7). For subwavelength particles, the sum converges after the first two terms, confirming the only the low-order terms (ka << 1) dominate. For larger targets, convergence requires summation of higher order terms, consistent with ka >> 1, where a is the object radius.

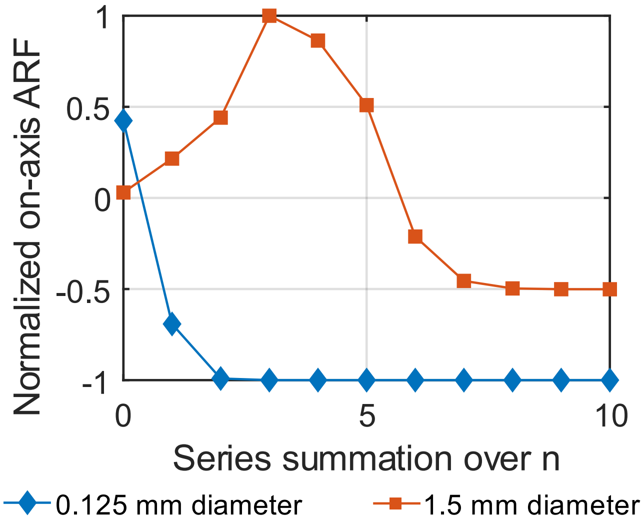

Figure S7: Cumulative series sum of radiation forces over index n. The multipole expansion series sum compares convergence for subwavelength objects *ka* << 1 (blue line) vs. *ka* ≳ 1 (orange line). For subwavelength target the radiation forces converge after the first two terms, while for objects > λ require higher order summation for convergence.

2. *Directivity correction effect on ARF*

The ARF results were compared for beam $P_{14}^{4}(cos\ \theta)$ with *M* = 3 on a 0.1-, 2-, and 6-mm glass spheres. Figure S8 demonstrates the ARF changes used in calculating the percent changes in Figure 4 of the manuscript.

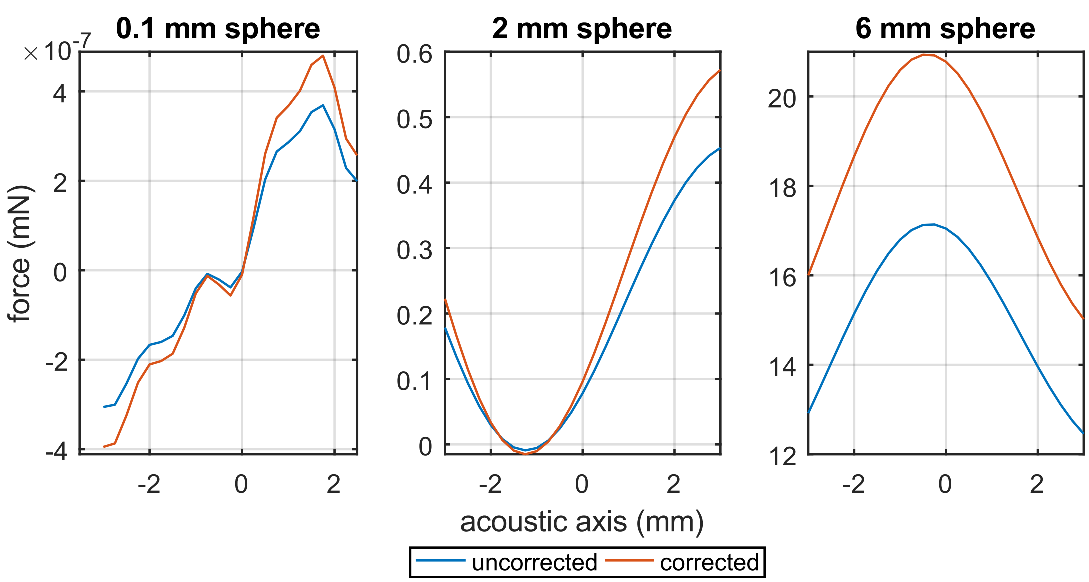

Figure S8: Acoustic radiation forces from $P_{14}^{4}(cos\ \theta)$ with *M* = 3 on different glass spheres located on the acoustic axis with (orange) and without (blue) directivity correction.

3. *Lateral ARF component from elements' asymmetric layout*

The asymmetry of the elements' layout produces lateral ARF that displaces the sphere from its on-axis position, thereby reducing the negative forces. As described in the Acoustic Beam section, vortex beams carry angular momentum, and two pulses of opposite helicity are transmitted consecutively to eliminate the resulting torque. However, the asymmetric placement of the array elements causes the lateral forces produced by each vortex helicity to be unequal, such that their average does not cancel to zero but instead yields a residual net lateral ARF, which also implies a nonzero net torque. This is evidenced by the nonzero lateral ARF shown in Figure S9c. Figure S9 shows the forces resulting from M = +3 (counterclockwise vortex), M = -3 (clockwise vortex), and their average, which exhibits a net lateral ARF. In conventional trapping, such lateral displacement of the sphere from the center is counteracted by a restoring force that returns it to its equilibrium position, as demonstrated in our previous work [11]. Here, however, the lateral ARF-induced perturbation of the sphere from its on-axis position reduces substantially the pulling force.

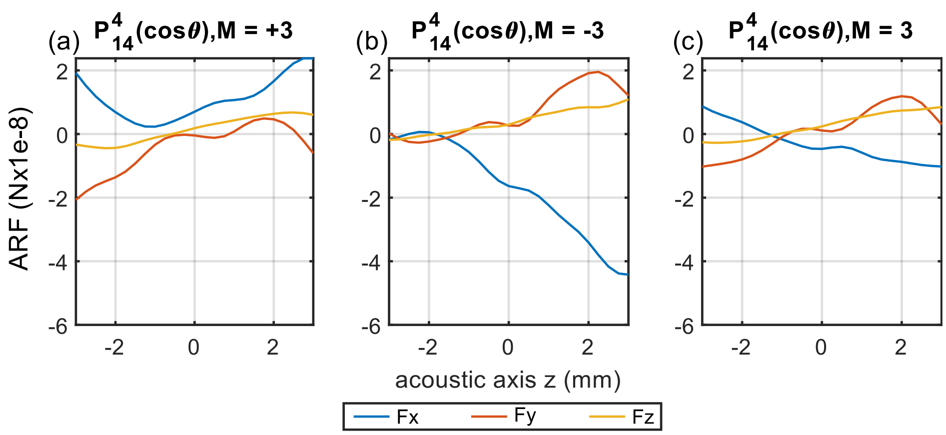

Figure S9: Transducer axial asymmetry resulting in a net lateral acoustic radiation force. The resulting ARFs from different vortex helicity: counterclockwise M = +3 (left), clockwise M = -3 (middle), and their average (right) show a net remaining lateral force. This force can displace the target from its on-axis position to a location with weaker negative radiation forces.

4. *Experimental demonstration of pulling a 2-mm glass sphere with $P^2_{11}(\theta)$ with M = 3*

Supplemental Movies S1 and S2 illustrate the experimental setup used to pull a glass sphere in a horizontal configuration. Movie S1 is recorded with a camera placed outside the water tank, while Movie S2 is recorded with a borescope camera placed inside the water tank, near the target. The ultrasound field propagates from left to right. A rectangular 12 × 10 × 1 cm gel slab made from UltraPure™ Low Melting Point Agarose (Thermo Fisher Scientific, Waltham, MA, USA), with a 5-mm-diameter tunnel through its center, is placed in a holder and submerged in degassed water. A 2-mm glass sphere, painted black, is placed inside the tunnel, with acoustically transparent anti-streaming membranes closing the tunnel's ends. An ultrasound imager (P6-3, Philips) was used to align the tunnel with the acoustic axis of the transducer, with the sphere positioned prefocally, where pushing forces are present. Initially, when the ultrasound is transmitted, the sphere is pushed away from the transducer against the anti-streaming membrane at the distal end of the tunnel. A stepper motor moves the whole transducer slowly, at 0.5 mm/sec, to the left, away from the sphere, until the sphere falls within the pulling region of the fusiform beam. As the transducer continues moving to the left, the sphere follows its motion.

As expected, we initially observed the sphere being pushed away from the transducer; slight pulling then occurred for approximately 1 millimeter (at timestamps 33 and 35 seconds in Movie S1 and S2, respectively), followed by pushing forces again. This second pushing phase indicates that the sphere exited the pulling region of the beam; however, the motion was too minimal to confirm a clear demonstration of pulling. As mentioned in the Discussion, difficulties in demonstrating pulling are related to the high acoustic power demand, which exceeded the transducer output, and to perturbation of the sphere from its on-axis position due to the lateral force component. There are additional difficulties specific to this setup, including possible misalignment between the acoustic axis and the transducer's motion axis, which can cause mispositioning of the sphere relative to the pulling region. The impedance mismatch as the wave travels from water to agarose to the water-filled tunnel causes refraction at each interface, following Snell's law. Because the field is focused, different rays arrive at these interfaces with different angles of incidence, so each ray is refracted by a different amount; this differentially perturbs the trap and lowers the pulling efficiency. Imperfections in the tunnel geometry, or even partial melting of the agarose gel from the acoustic exposure, may also have contributed to these difficulties.

Thermal limits of the transducer prevented running the experiment for longer than 60 seconds consecutively, which otherwise could have allowed repositioning of the setup to find the optimal alignment.

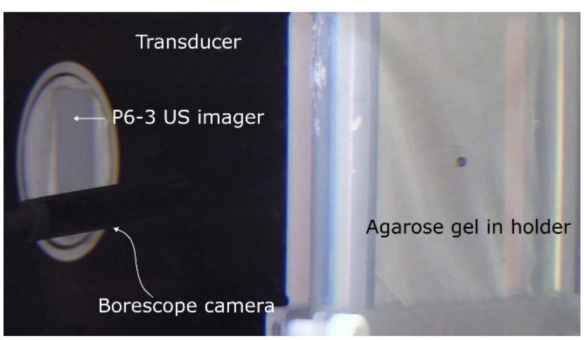

Movie S1: Experimental trial in a horizontal configuration, recorded with a camera placed outside the water tank.

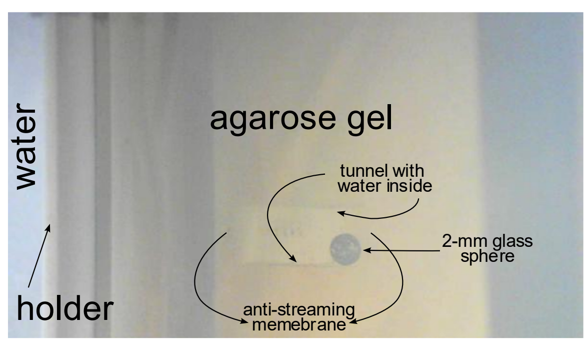

Movie S2: Experimental trial in a horizontal configuration, recorded with a borescope camera. Slight motion toward the transducer occurs at timestamp 35 s. Challenges related to centering, axis alignment, trap perturbations, and transducer thermal limits made consistent demonstration of pulling difficult.

Appendix A: Acoustic radiation force equations

The mathematical framework for the acoustic radiation forces discussed in this work is adapted from reference [10]. The following equations represent the main functional forms for reference, omitting the full derivation for the sake of brevity.

The acoustic radiation forces on a spherical scatterer in an arbitrary waveform are defined as:

$$F_x = \frac{1}{8\pi^2 \rho c^2 k^2} \mathrm{Re}\left\{\sum_{n=0}^{\infty} \Psi_n \sum_{n=0}^{\infty} A_{nm}\left(H_{nm}H_{n+1,m+1}^{*} - H_{n,-m}H_{n+1,-m-1}^{*}\right)\right\}$$

$$F_y = \frac{1}{8\pi^2 \rho c^2 k^2} \mathrm{Im}\left\{\sum_{n=0}^{\infty} \Psi_n \sum_{n=0}^{\infty} A_{nm}\left(H_{nm}H_{n+1,m+1}^{*} + H_{n,-m}H_{n+1,-m-1}^{*}\right)\right\}$$

$$F_z = \frac{-1}{4\pi^2 \rho c^2 k^2} \mathrm{Re}\left\{\sum_{n=0}^{\infty} \Psi_n \sum_{n=0}^{\infty} B_{nm}H_{nm}H_{n+1,m}^{*}\right\}$$

with the following

$$\Psi_n = (1 + 2c_n)(1 + 2c_n^{*}) - 1$$

$$A_{nm} = \sqrt{\frac{(n+m+1)(n+m+2)}{(2n+1)(2n+3)}}$$

$$B_{nm} = \sqrt{\frac{(n+m+1)(n+m+1)}{(2n+1)(2n+3)}}$$

$$H_{nm} = \iint_{k_x^2+k_y^2 \le k^2} dk_x dk_y S_{corr}(k_x, k_y) Y_{nm}^{*}(\theta_k, \varphi_k)$$

where Y_{nm} and c_n are spherical harmonics, and spherical scattering coefficients.

References

[1] P. L. Marston, “Axial radiation force of a Bessel beam on a sphere and direction reversal of the force,” *J. Acoust. Soc. Am.*, vol. 120, no. 6, pp. 3518–3524, 2006, doi: 10.1121/1.2361185.

[2] W. Magnus and F. Oberhettinger, *Formulas and Theorems for the Functions of Mathematical Physics*, First. New York: Chelsea Publishing Company, 1943.

[3] M. A. Ghanem, A. D. Maxwell, O. A. Sapozhnikov, V. A. Khokhlova, and M. R. Bailey, “Quantification of acoustic radiation forces on solid objects in fluid,” *Phys. Rev. Appl.*, vol. 12, no. 4, p. 44076, Oct. 2019, doi: 10.1103/PhysRevApplied.12.044076.

[4] M. R. Dennis and J. B. Götte, "Instability of higher-order optical vortices analyzed with multi-pinhole interferometer," *Phys. Rev. Lett.*, vol. 109, no. 18, pp. 1018–1020, 2012, doi: 10.1103/PhysRevLett.109.183903.

[5] L. Zhang and P. L. Marston, "Acoustic radiation torque on small objects in viscous fluids and connection with viscous dissipation," *J. Acoust. Soc. Am.*, vol. 136, no. 6, pp. 2917–2921, 2014, doi: 10.1121/1.4900441.

[6] B. Hefner and P. Marston, "An acoustical helicoidal wave transducer with applications for the alignment of ultrasonic and underwater systems," *J. Acoust. Soc. Am.*, vol. 106, pp. 3313–3316, 1999, doi: 10.1121/1.428184.

[7] L. Zhang and P. L. Marston, "Angular momentum flux of nonparaxial acoustic vortex beams and torques on axisymmetric objects," *Phys. Rev. E Stat. Nonlin. Soft Matter Phys.*, vol. 84, no. 6, Dec. 2011, doi: 10.1103/PhysRevE.84.065601.

[8] A. Marzo, M. Caleap, and B. W. Drinkwater, "Acoustic virtual vortices with tunable orbital angular momentum for trapping of Mie particles," *Phys. Rev. Lett.*, vol. 120, p. 44301, 2018, doi: 10.1103/PhysRevLett.120.044301.

[9] M. A. Ghanem *et al.*, "Field characterization and compensation of vibrational nonuniformity for a 256-element focused ultrasound phased array," *IEEE Trans. Ultrason. Ferroelectr. Freq. Control*, vol. 65, no. 9, pp. 1618–1630, 2018, doi: 10.1109/TUFFC.2018.2851188.

[10] O. A. Sapozhnikov and M. R. Bailey, "Radiation force of an arbitrary acoustic beam on an elastic sphere in a fluid," *J. Acoust. Soc. Am.*, vol. 133, no. 2, pp. 661–676, 2013, doi: 10.1121/1.4773924.

[11] M. A. Ghanem *et al.*, "Noninvasive acoustic manipulation of objects in a living body," *Proceedings of the National Academy of Sciences*, vol. 117, no. 29, pp. 16848 LP – 16855, Jul. 2020, doi: 10.1073/pnas.2001779117.